Micromechanical Characterization of $Ce_{0.8}Gd_{0.2}O_{2-\delta}$–$FeCo_2O_4$ Dual Phase Oxygen Transport Membranes

Fanlin Zeng,* Jürgen Malzbender, Stefan Baumann, Falk Schulze-Küppers, Manja Krüger, Arian Nijmeijer, Olivier Guillon, and Wilhelm Albert Meulenberg

Aiming toward an optimization of dual phase oxygen transport membrane materials for oxygen separation applications, ceramic composites consisting of a $Ce_{1-x}Gd_xO_{2-\delta}$ $(0 < x < 0.2)$ fluorite phase, $Gd_{0.9}Ce_{0.1}Fe_{0.8}Co_{0.2}O_3$ perovskite phase, $Fe_xCo_{3-x}O_4$ $(0 < x < 1)$ spinel phase, and CoO rock salt phase are developed and micromechanical properties (elastic modulus and hardness) of $xCe_{0.8}Gd_{0.2}O_{2-\delta}$: $(1-x)FeCo_2O_4$ (50 wt% $\leq x \leq$ 90 wt%) composites are characterized via indentation testing at room temperature. The results obtained at low indentation loads indicate that the magnitude of the elastic moduli of the different phases is in the order $Gd_{0.9}Ce_{0.1}Fe_{0.8}Co_{0.2}O_3 > Ce_{1-x}Gd_xO_{2-\delta} \approx Fe_xCo_{3-x}O_4 > CoO$, and furthermore, hardness values are also in the same order. The hardness values of the obtained composites at higher impression loads reveal a stronger dependency on porosity than on composition due to similar hardness values of the main phases. Any compositional effect appears to diminish above a porosity of $\approx$1%.

1. Introduction

Oxygen transport membranes, which exhibit an almost 100% permeation selectivity regarding oxygen,[1] are a promising option to realize environmental-friendly, economically sound, and efficient processes for pure oxygen production,[1–4] oxy-combustion,[5–7] and conversion of carbonaceous products.[8–12] These applications typically involve harsh environments, in particular high temperatures, and oxygen partial pressure gradients as well as the exposure to flue gas, which can be detrimental to the

chemical and mechanical stability of the respective membrane components.[13,14]

Ceramic dual phase oxygen transport membranes are promising candidates for long-term stable operation under application-relevant conditions.[15–19] These dual phase membranes consist of two separated phases responsible for ionic and electronic conductivity, respectively.[1] Flexible tailoring regarding chemical properties and stability is permitted by a choice of plenty of possible materials for the individual phases with sufficient ionic or electronic conductivity.[20–23]

In fact, it has been indicated that the use of $Ce_{0.8}Gd_{0.2}O_{1.9}$ as an ionic conducting phase enables the formation of mechanically and chemically stable composites.[15,18,24–26] Furthermore, it appears that the performance of $Ce_{0.8}Gd_{0.2}O_{1.9}$-based dual phase membranes can benefit from phase interactions between the two phases in the composites.[27,28]

To limit thermal stresses that might induce microcracking and failure, the selection of an electronic conducting phase for $Ce_{0.8}Gd_{0.2}O_{1.9}$-based dual phase membranes should be based not only on performance regarding conductivity, but also on a matching coefficient of thermal expansion (TEC) with that of $Ce_{0.8}Gd_{0.2}O_{1.9}$. Therefore, $FeCo_2O_4$ is an excellent candidate because of its high electronic conductivity of $18 \, S \, cm^{-1}$ at 800 °C. Furthermore, it possesses a TEC that is close to that of $Ce_{0.8}Gd_{0.2}O_{1.9}$ ($\approx 12 \times 10^{-6} \, K^{-1}$).[13]

In fact, composites of $xCe_{0.8}Gd_{0.2}O_{2-\delta}$: $(1-x)FeCo_2O_4$ (60 wt% $\leq x \leq$ 90 wt%) (CGO20–FC2O) have been reported to possess a remarkable chemical stability under flue gas conditions.[19] These composites are multiphase systems consisting of a $Ce_{1-x}Gd_xO_{2-\delta}$ $(0 < x < 0.2)$ (CGO) fluorite phase, an $Fe_xCo_{3-x}O_4$ $(0 < x < 1)$ (FCO) spinel phase, a (Fe,Co)O rock salt phase, and a $Gd_{0.85}Ce_{0.15}Fe_{0.75}Co_{0.25}O_3$ (GCFCO) perovskite phase formed via phase reaction between $Ce_{0.8}Gd_{0.2}O_{2-\delta}$ (CGO20) and $FeCo_2O_4$ (FC2O).[19,28] In this case, the newly formed electronic conductive phases, i.e., (Fe,Co)O and GCFCO, contribute to an improved ambipolar conductivity.[19,28]

There are a number of reports on the mechanical properties of single phase oxygen transport membranes;[29–33] however, studies on the mechanical properties of dual phase membranes are limited.[18,34,35] Currently no study has been reported on the mechanical properties of CGO20–FC2O composites. Therefore, in this work, we report on the investigation of the mechanical

F. Zeng, Dr. J. Malzbender, Dr. S. Baumann, Dr. F. Schulze-Küppers, Prof. M. Krüger, Prof. O. Guillon, Prof. W. A. Meulenberg
Institute of Energy and Climate Research (IEK)
Forschungszentrum Jülich GmbH
Jülich 52425, Germany
E-mail: f.zeng@fz-juelich.de

F. Zeng, Prof. A. Nijmeijer, Prof. W. A. Meulenberg
Inorganic Membranes, MESA+ Institute for Nanotechnology
University of Twente
P.O. Box 217, Enschede 7500 AE, The Netherlands

**ADVANCED
SCIENCE NEWS**
www.advancedsciencenews.com

**ADVANCED
ENGINEERING
MATERIALS**
www.aem-journal.com

properties of initial CGO20–FC2O composites and subsequently formed phase components by indentation testing. The grain sizes of individual phases in the composites were optimized for the mechanical property assessment via indentation testing. The relationships between mechanical properties of the composites and compositional variations as well as porosities are discussed.

2. Results and Discussion

2.1. Phase and Microstructure Characterizations

As the first step, the phase components of composites were investigated via X-ray diffraction (XRD). The XRD patterns of CGO20–FC2O and CGO20–FCO$_L$ reveal the coexistence of CGO fluorite, GdFeO$_3$-type perovskite, CoO rock salt, and FCO spinel with variations in the cobalt/iron ratio (see Figure S1, Supporting Information). The lattice parameters of the individual phases except the FCO spinel phase in CGO20–FC2O and CGO20–FCO$_L$ appear to be rather independent of composition (see Table S1, Supporting Information), whereas the XRD pattern of CGO20–GCFCO confirms the presence of only CGO fluorite and GdFeO$_3$-type perovskite phases, which indicates a successfully synthesized dual phase composite membrane. Furthermore, the lattice parameter of the GdFeO$_3$-type perovskite is close to those of the CGO20–FC2O composites.

Microstructures of the polished cross-sections of the composite are shown in **Figure 1**a–h. Three phases are distinguishable either by intensity or by topography. Some grains are concave possibly due to differences in elastic, plastic, and fracture properties. The gray grains, denoted as 1, appear to be CGO grains in all composites, as determined via energy-dispersive X-ray spectroscopy point quantification. These grains only contain Ce and Gd (see Table S2, Supporting Information). The Ce/Gd ratios in CGO are nearly the same in CGO20–FC2O and CGO20–FC2O$_L$, while the Ce/Gd ratios in CGO in CGO20–GCFCO are slightly larger. The investigated black grains, denoted as 2, in CGO20–FC2O and CGO20–FC2O$_L$ consist of Co and Fe only. They are characterized as being FCO with varying Fe/Co content. The concave grains, denoted as 3, are composed of mainly Gd and Fe, which indicates that they are GdFeO$_3$-type perovskite grains.

The element ratios indicate that the GdFeO$_3$-type perovskite in CGO20–FC2O and CGO20–FC2O$_L$ is doped by Ce and Co at the A and B sites,[28] and the molar ratio of $(Gd + Ce)/(Fe + Co)$ is approximately equal to 1 (see Table S2, Supporting Information). Consequently, the composition of the GdFeO$_3$-type perovskite in CGO20–FC2O and CGO20–FC2O$_L$ is estimated to be Gd$_{0.9}$Ce$_{0.1}$Fe$_{0.8}$Co$_{0.2}$O$_3$ (GCFCO) within the assessed grains. However, the composition of the investigated GdFeO$_3$-type perovskite grains in CGO20–GCFCO is estimated to be Gd$_{0.9}$Ce$_{0.1}$FeO$_3$ (GCFO) and contains no Co. The similar lattice parameters of GCFCO and GCFO can be seen as indication of similar chemical bonding strengths between atoms; this might already imply that GCFCO and GCFO possess similar elastic moduli and hardness values.

Nevertheless, the rock salt phase CoO could not be detected via backscattered electron microscopy (BSEM). Thus, additional electron backscatter diffraction (EBSD) measurements were performed on CGO20–FC2O to quantify all the phases. An example of the EBSD phase mapping result for 50CGO20–FC2O is shown in **Figure 2**. Four phases are detected via EBSD, including CGO fluorite, GCFCO perovskite, CoO rock salt, and FCO spinel, which is in good agreement with the XRD results. The minor phase, i.e., GCFCO and CoO, in 50CGO20–FC2O appears to be rather inhomogeneously distributed in a 2D image (see Figure 2). It should be noted that some small grains or small grain surfaces might be not identified correctly under the current resolution. Moreover, 3D reconstructions were not yet successful due to complexity, i.e., four phases of similar compositions with small grain size. Further analysis is necessary to clarify the exact phase evolution and distribution.

The volume fractions of all individual phases in CGO20–FC2O are shown in **Figure 3**. The average grain sizes of the respective phases are summarized in **Table 1**. CGO is the most prominent phase with the highest volume fraction, possessing a grain size of 0.5 μm in the investigated composites. FCO is the second-most abundant phase, with grain sizes close to that of CGO. The GCFCO volume fraction increases marginally with CGO20/FC2O ratio, with a maximum at a CGO20 content of 85 wt%. The grain size of GCFCO decreases slightly with increasing CGO20 content. A small amount of CoO phase is only detectable in 50CGO20–FC2O and 60CGO20–FC2O with grain sizes similar to that of CGO.

It should also be noted that the volume fraction of the GCFCO phase in these small grains might be underestimated because of a topography effect of grain boundaries from the concave grains (Figure 1).

2.2. Mechanical Properties

The indentation technique provides a convenient characterization method of the mechanical properties from macroscale to nanoscale,[36] creating the capability to obtain macroscopically and nondestructively the local mechanical properties of individual phases in composites via imprints with dimensions restrained to ≈1/10 or less of the size of a targeted single grain or an isolated phase area, i.e., less than 50 nm for CGO20–FC2O. It is not possible to locate imprints on grains smaller than ≈2 μm via the available optical microscope with a 50× objective lens.

Therefore, CGO20–GCFCO and CGO20–FC2O$_L$ materials with larger grain sizes were used for targeted indentation tests with a load of 5 mN to characterize the mechanical properties of the individual phases. The tests were conducted for individual grains (such as the grain denoted as 2 in Figure 1g and 4 in Figure 1h, respectively) or phase areas (such as the area denoted as 1 in Figure 1g) with a diameter larger than 6 μm, because they can be expected to be more than ten times larger than the indentation sizes (plastic and elastic zone) and can therefore be easily identified by color and topography with the optical microscope.

For CGO20–GCFCO, indents were located close to the centers of 20 concave GCFCO grains, and for CGO20–FC2O$_L$, indentations were initially located close to the centers of 20 isolated white CGO phase areas. Subsequently, to identify mechanical properties of FCO and CoO grains, special indentation test schedules were developed combined with EBSD investigations on indented areas, as outlined in the following.
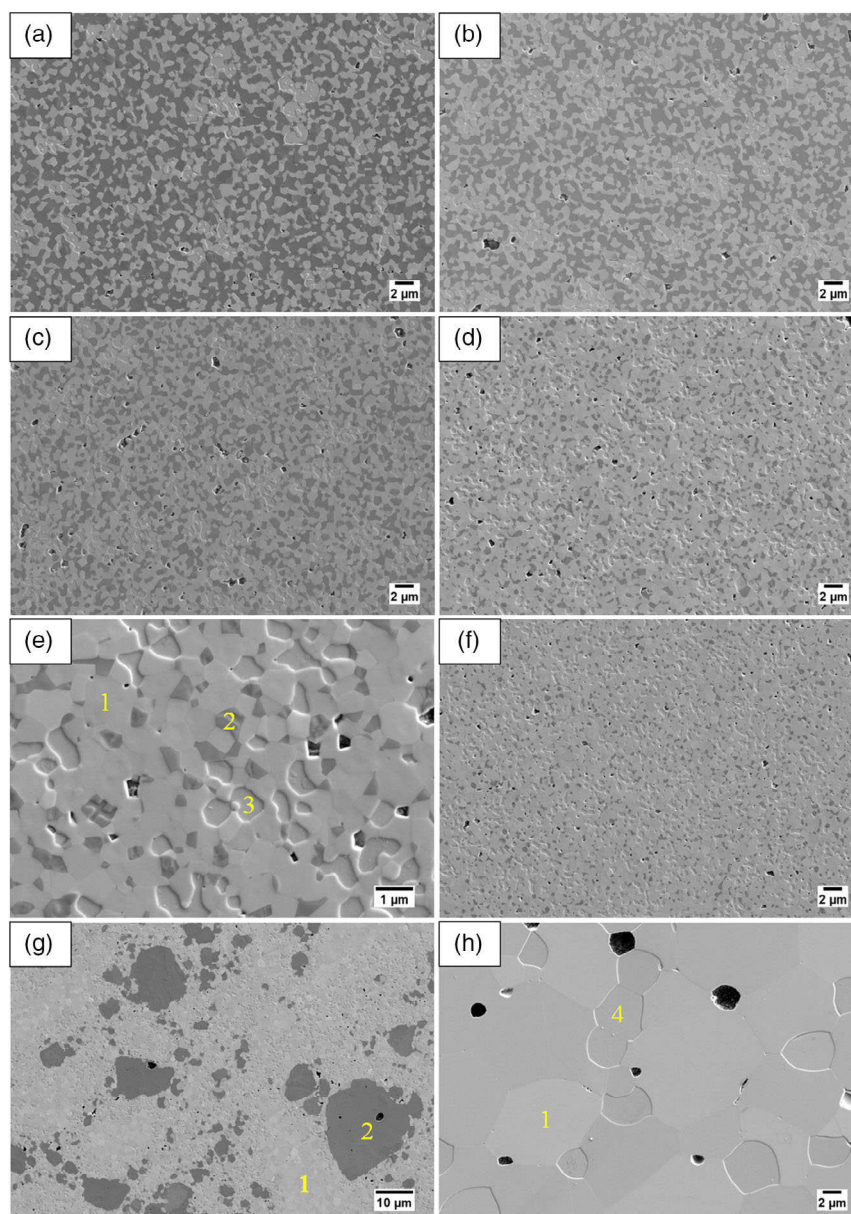
Figure 1. Microstructures of a) 50CGO20–FC2O, b) 60CGO20–FC2O, c) 70CGO20–FC2O, d) 85CGO20–FC2O, e) 85CGO20–FC2O with lager magnification and labeled grains, f) 90CGO20–FC2O, g) CGO20–FCO$_L$, and h) CGO20–GCFCO (CGO, FCO, GCFCO, and GCFO are denoted as 1, 2, 3, and 4, respectively).

A 15 × 15 grid of indentations with a load of 5 mN was imprinted on CGO20–FC2O$_L$, where in particular large black grains were selected. The distance between each indent was set to ≈3 μm, which is approximately three times larger than the indentation sizes (<1 μm) to minimize influence from neighboring imprints.[37,38] The indented areas were afterward characterized via EBSD to verify phases.

The phase mapping of the indented area is shown in **Figure 4**b for comparison along with an optical micrograph (Figure 4a). It shows that the brownish grains are FCO grains (Figure 4a), and most CoO grains visible as grayish are embedded within the FCO grains. Therefore, the large gray grains inside brownish FCO

grains could be targeted as CoO grains for the indentation tests under the optical microscope.

The derived elastic modulus *(E)* and hardness (*H*) mappings of the grid of imprints are presented in Figure 4c,d, respectively. Some indents were located on cracks, grain boundaries, and pores, leading to low *E* and *H* values. These artifacts will not be considered during the subsequent analysis and discussion.

The CoO grains have an *E* value close to that of the FCO grains, which is lower than the *E* value of their surrounding grains (CGO and GCFCO), whereas the *H* value of the CoO grains is much lower than the *H* value of FCO.
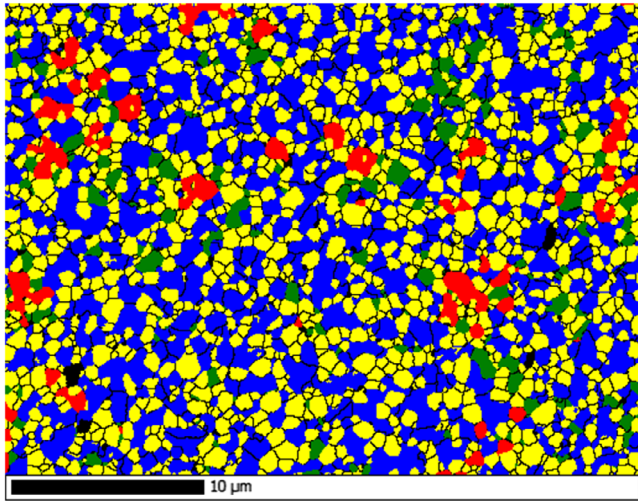
**ADVANCED
SCIENCE NEWS**
www.advancedsciencenews.com

**ADVANCED
ENGINEERING
MATERIALS**
www.aem-journal.com

Figure 2. EBSD phase mapping on 50CGO20–FC2O: the yellow, red, blue, and green phase are CGO, GFCCO, FCO, and CoO, respectively.
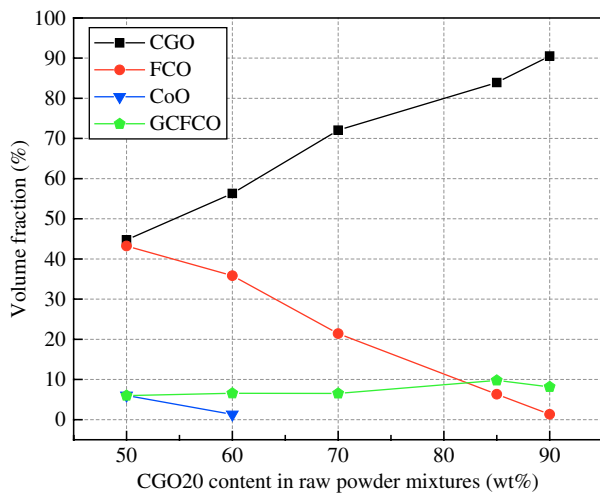

Figure 3. Volume fractions of the individual phases in CGO20–FC2O.

Table 1. Average grain sizes of phases in CGO20–FC2O.

Grain size Composite	CGO [μm]	FCO [μm]	GCFCO [μm]	CoO [μm]
50CGO20–FC2O	0.5 ± 0.2	0.7 ± 0.4	1.0 ± 0.5	0.5 ± 0.2
60CGO20–FC2O	0.5 ± 0.2	0.6 ± 0.3	0.8 ± 0.4	0.4 ± 0.2
70CGO20–FC2O	0.5 ± 0.2	0.5 ± 0.2	0.5 ± 0.2	–
85CGO20–FC2O	0.5 ± 0.2	0.3 ± 0.1	0.4 ± 0.2	–
90CGO20–FC2O	0.5 ± 0.2	0.3 ± 0.1	0.4 ± 0.1	–

To get statistically relevant values of the mechanical properties of the FCO and CoO phases, indents were subsequently imprinted in an additional test series in the middle of a number of individual grains, including 50 FCO grains and 20 CoO grains. Because of the variations in cobalt content, a higher number of FCO grains were investigated to derive reliable statistical values.

The derived mechanical properties of the individual phases are summarized in **Table 2**. The E and H values of GCFO are significantly larger than those of the other phases, and they are the same as for GCFCO. CGO and FCO show similar E and H values within the limits of statistical uncertainty. CoO possesses a similar elastic modulus, but a much lower hardness, when compared with CGO and FCO. Furthermore, the mechanical properties of FCO are barely influenced by variations in cobalt content as the standard deviations of the E and H values of FCO are close to that of CGO. These deviations might be induced by the noise in the device.[39] In summary, the E values decrease according to GCFCO ≈ GCFO > CGO ≈ FCO > CoO, and the H values descend in the same order.

Therefore, on the basis of mechanical properties and volume fractions of the phase constituents in CGO20–FC2O, it can be predicted that the elastic modulus and hardness of CGO20–FC2O improve as a function of CGO content due to the associated increase in CGO and GCFCO content in the composites (Figure 3), whereas the small amount of CoO rock salt phase is expected to have only a minor effect.

To assess the average elastic modulus and hardness of CGO20–F2CO considering it as a kind of homogeneous material, imprints should be significantly larger than the representative volume element of the composites.[40] The small grain size and good homogeneity of the individual phases in CGO20–F2CO suggest that imprints with a size around ten times larger (>5 μm) than the grain size will be appropriate for yielding a reliable effective elastic modulus and hardness for the composites. Thus, 20 indentation tests with a higher load of 150 mN were conducted on the polished sample cross-sections in subsequent tests. The resulting imprints were larger than 5 μm and covered a representative area of the microstructure of the composites.

The derived mechanical properties for the CGO20–FC2O composite are shown in **Figure 5**. The E value starts to rise marginally when the CGO phase is above 72 vol%, whereas the H value shows no clear dependence on CGO content but shows a minimum value when CGO is 72 vol%, coinciding with the highest porosity obtained for the range of compositions in this work.

Usually, both the E value and H value of ceramic materials decrease with increasing porosities.[31,41] The porosities of CGO20–FC2O except 70CGO20–FC2O vary between ≈0.6% and ≈0.7% (Figure 5), and they barely change with composition, whereas 70CGO20–FC2O has a relatively higher porosity of ≈1.3%, which leads to a slight decrease of the H value but no significant influence on the E value. Thus, the dependence of the H value on porosity is stronger than that of the E value, and the E value is more dependent on composition (note, the elastic zone is around ten times larger than the plastic zone; therefore, the hardness is more strongly affected by local effects).

In the interest of validating the influence of porosities on indentation test results, an 85CGO20–FC2O composite with a higher porosity of ≈3.8% but with the same composition, abbreviated as 85CGO20–FCO_P, was prepared by a Pechini process. Details of the synthesis route and microstructure were reported elsewhere.[6] Both the E value and the H value of 85CGO20–FCO_P, as derived from the indentation tests with a load of 150 mN, are smaller than the values obtained for the 85CGO20–FC2O composition (**Table 3**). They are even lower than that of 50CGO20–FC2O with a porosity of 0.6% despite the high
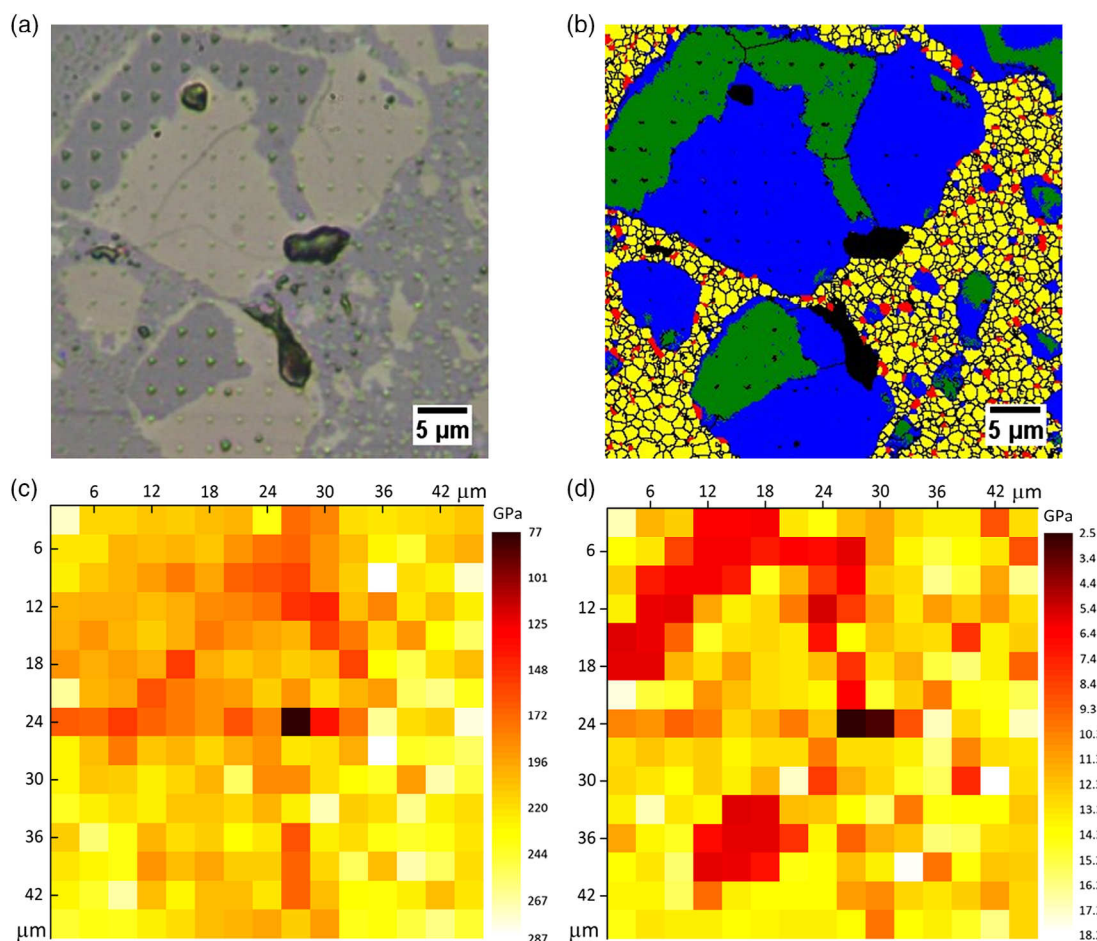
Figure 4. Investigation of grid indentation array via a) optical micrograph, b) EBSD phase mapping (the blue, green, yellow, and red grains correspond to FCO, CoO, CGO, and GCFCO, respectively), and the corresponding c) elastic modulus mapping and d) hardness mapping.

Table 2. Mechanical properties of CGO, FCO, CoO, and GCFO phases.

Property Phase	Elastic modulus [GPa]	Hardness [GPa]
GCFO	284 ± 21	31.7 ± 1.9
CGO	229 ± 10	13.6 ± 0.7
FCO	209 ± 12	13.3 ± 0.8
CoO	193 ± 17	6.1 ± 0.6

CGO and GCFCO content. Therefore, it can be concluded that the porosity has a stronger effect than the composition on the elastic modulus and hardness of CGO20–FC2O when the porosity exceeds ≈1%.

Figure 5. Elastic modulus, hardness, and porosities of CGO20–FC2O.

3. Conclusions

Four phases, including CGO, GCFCO, FCO, and CoO, were identified in CGO20–FC2O composites, which were synthesized by solid state react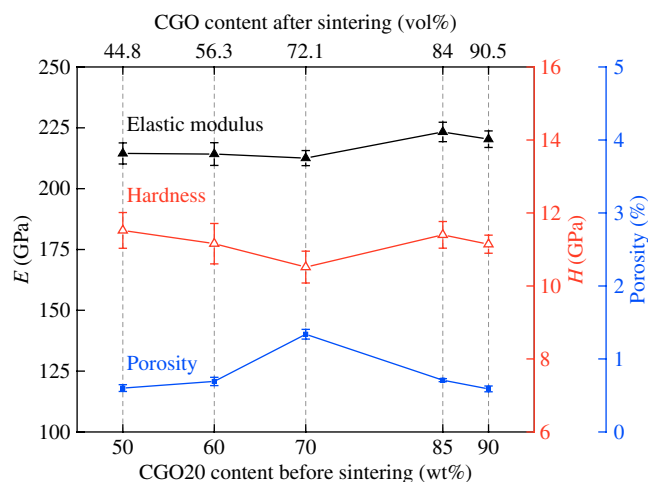ion. Their individual elastic modulus and hardness values are derived from targeted indentation measurements on composites with optimized microstructures. The results indicate that the E values decrease according to

**ADVANCED
SCIENCE NEWS**

www.advancedsciencenews.com

**ADVANCED
ENGINEERING
MATERIALS**

www.aem-journal.com

Table 3. Mechanical properties of 85CGO20–FC2O with different porosities.

Property	Porosity [%]	Elastic modulus [GPa]	Hardness [GPa]
Composite			
85CGO20–FC2O	0.7 ± 0.02	223 ± 4	11.4 ± 0.4
85CGO20–FC2O$_P$	3.8 ± 1.7	196 ± 5	9.7 ± 0.5

$GCFCO > CGO \approx FCO > CoO$, and the H values descend in the same order. The E value mainly depends on the composition, and slightly increases with CGO content, whereas the H value is biased to a stronger extent by porosity rather than composition. Furthermore, it can also be concluded from indentation test results that a porosity above $\approx 1\%$ has a stronger effect on the elastic modulus and hardness than the composition for CGO20–FC2O composites. Overall, this work provides the elastic modulus and hardness of all individual phases in CGO20–FC2O materials, including apparently high-temperature stable phases and phase interaction products. The results can be applied for further mechanical modeling.

4. Experimental Section

All powders were manufactured by mixing of stoichiometric amounts of $Ce_{0.8}Gd_{0.2}O_{1.9}$ (CGO20) (Treibacher Industrie AG, 99%), Co_3O_4 (Merck, 99%), and Fe_2O_3 (Merck, 99%) (the mole ratio of Co_3O_4/Fe_2O_3 was fixed at 4:3 to form $FeCo_2O_4$ spinel (FC2O)) via ball milling in ethanol. The powder mixtures were dried at 75 °C for 3 days, and then they were uniaxially pressed into discs and sintered at 1200 °C for 10 h in air to obtain CGO20–FC2O composites.[6] Finally, five CGO20/FC2O ratios were synthesized, and they were abbreviated as 50CGO20–FC2O, 60CGO20–FC2O, 70CGO20–FC2O, 85CGO20–FC2O, and 90CGO20–FC2O with weight fractions of CGO20 in raw powder mixtures equal to 50, 60, 70, 85, and 90 wt%, respectively.

Two other kinds of powder mixtures were also prepared to obtain composites with grains as large as 6 μm. One was used to sinter composites with large FCO grains. It was mixed by 85 wt% CGO20 and 15 wt% manually crushed and milled FC2O particles from bulk FC2O samples. The sintered composite was named CGO20–FC2O$_L$. The other powder mixture was used to prepare a composite with large GCFCO grains sintered at 1500 °C for 10 h. The cobalt and iron oxides in the powder mixtures were restrained to an amount needed to form the GCFCO phase to reduce the amount of a liquid phase formed at high temperatures.[27,42] This amount was calculated by assuming no oxygen loss or gain in the powder mixtures after sintering according to the reported compositions for 85CGO20–FC2O.[13] The sintered composite with only CGO and GCFCO was named CGO20–GCFCO.

The sintered samples were embedded in resin and ground with SiC paper to remove the as-sintered surface. Then the ground samples were polished in a colloidal silica solution for at least 4 h until all scratches were removed.

Crystalline structure characterization, phase composition determination and quantification were performed via XRD (Empyrean, Malvern Panalytical Ltd). The instrument was equipped with a Cu long fine focus tube, Bragg-Brentano^{HD} mirror, and PIXcel3D detector. Microstructures, including grain size and volume fraction, were assessed with BSEM (Merlin, Carl Zeiss Microscopy Ltd) and EBSD (NordlysNano, Oxford Instruments Ltd). The porosities of the samples were calculated as area fraction of pores measured via the ImageJ software based on binary pictures of polished sample cross-sections from at least three BSEM images via the so-called isodata threshold method.[43,44]

Instrumented indentation tests (NanoTest Xtreme, Micro Materials Ltd) were performed on polished samples according to ASTM E2546-15[45] using a constant loading/unloading time of 10 s and a holding time of 8 s. The number of measurements is specified in the Results and Discussion section. The positioning of the imprint was assisted by an optical microscope equipped with an objective lens of 50×, where large pores and cracks were avoided. The mechanical properties were then deduced according to the methodology proposed by Oliver and Pharr.[46]

Conflict of Interest

The authors declare no conflict of interest.

[1] X. Zhu, W. Yang, *Mixed Conducting Ceramic Membranes*, Springer, Dalian, China **2017**.

[2] P. Niehoff, F. Schulze-Kueppers, S. Baumann, W. A. Meulenberg, O. Guillon, R. Vassen, *Am. Ceram. Soc. Bull.* **2015**, *94*, 28.

[3] K. Zhang, J. Sunarso, Z. Shao, W. Zhou, C. Sun, S. Wang, S. Liu, *RSC Adv.* **2011**, *1*, 1661.

[4] H. Wang, S. Werth, T. Schiestel, J. Caro, *Angew. Chem., Int. Ed.* **2005**, *44*, 6906.

[5] H. Stadler, F. Beggel, M. Habermehl, B. Persigehl, R. Kneer, M. Modigell, P. Jeschke, *Int. J. Greenhouse Gas Control* **2011**, *5*, 7.

[6] M. Ramasamy, *Dual Phase Oxygen Transport Membrane for Efficient Oxyfuel Combustion*, Bochum University, Bochum, Germany **2016**.

[7] X. Zhu, H. Liu, Y. Cong, W. Yang, *Chem. Commun.* **2012**, *48*, 251.

[8] P.-M. Geffroy, J. Fouletier, N. Richet, T. Chartier, *Chem. Eng. Sci.* **2013**, *87*, 408.

[9] C. Karakaya, R. J. Kee, *Prog. Energy Combust. Sci.* **2016**, *55*, 60.

[10] H. Jiang, H. Wang, S. Werth, T. Schiestel, J. Caro, *Angew. Chem., Int. Ed.* **2008**, *47*, 9341.

[11] H. J. Bouwmeester, *Catal. Today* **2003**, *82*, 141.

[12] X. Dong, W. Jin, N. Xu, K. Li, *Chem. Commun.* **2011**, *47*, 10886.

[13] M. Ramasamy, S. Baumann, J. Palisaitis, F. Schulze-Küppers, M. Balaguer, D. Kim, W. A. Meulenberg, J. Mayer, R. Bhave, O. Guillon, *J. Am. Ceram. Soc.* **2016**, *99*, 349.

[14] L. L. Anderson, P. A. Armstrong, R. R. Broekhuis, M. F. Carolan, J. Chen, M. D. Hutcheon, C. A. Lewinsohn, C. F. Miller, J. M. Repasky, D. M. Taylor, *Solid State Ionics* **2016**, *288*, 331.

[15] H. Luo, H. Jiang, K. Efimov, F. Liang, H. Wang, J. R. Caro, *Indus. Eng. Chem. Res.* **2011**, *50*, 13508.

[16] S. Guo, Z. Liu, J. Zhu, X. Jiang, Z. Song, W. Jin, *Fuel Process. Technol.* **2016**, *154*, 19.

[17] H. Luo, K. Efimov, H. Jiang, A. Feldhoff, H. Wang, J. Caro, *Angew. Chem., Int. Ed.* **2011**, *50*, 759.

[18] S. Kim, S. H. Kim, K. S. Lee, J. H. Yu, Y.-H. Seong, I. S. Han, *Ceram. Int.* **2017**, *43*, 1916.

[19] M. Ramasamy, E. Persoon, S. Baumann, M. Schroeder, F. Schulze-Küppers, D. Görtz, R. Bhave, M. Bram, W. Meulenberg, *J. Membr. Sci.* **2017**, *544*, 278.

[20] B. C. Steele, *Curr. Opin. Solid State Mater. Sci.* **1996**, *1*, 684.

[21] V. Kharton, A. Kovalevsky, A. Viskup, A. Shaula, F. Figueiredo, E. Naumovich, F. Marques, *Solid State Ionics* **2003**, *160*, 247.

[22] A. Petric, H. Ling, *J. Am. Ceram. Soc.* **2007**, *90*, 1515.

[23] E. Verwey, P. Haayman, F. Romeijn, *J. Chem. Phys.* **1947**, *15*, 181.

[24] A. J. Samson, M. Søgaard, P. V. Hendriksen, *J. Membr. Sci.* **2014**, *470*, 178.

[25] W. Fang, F. Liang, Z. Cao, F. Steinbach, A. Feldhoff, *Angew. Chem., Int. Ed.* **2015**, *54*, 4847.

[26] M. Lipińska-Chwałek, F. Schulze-Küppers, J. Malzbender, *J. Eur. Ceram. Soc.* **2015**, *35*, 1539.

[27] Y. Lin, S. Fang, D. Su, K. S. Brinkman, F. Chen, *Nat. Commun.* **2015**, *6*, 6824.

[28] M. Ramasamy, S. Baumann, A. Opitz, R. Iskandar, J. Mayer, D. Udomsilp, U. Breuer, M. Bram, in *Advances in Solid Oxide Fuel Cells Electronic Ceramics II: Ceramic Engineering Science Proc.* (Eds: M. Kusnezoff, N. P. Bansal, K. Shimamura, M. Fukushima, A. Gyekenyesi), Vol. *37*, Wiley, Florida **2017**, pp. 99–112.

[29] G. Pećanac, S. Baumann, J. Malzbender, *J. Membr. Sci.* **2011**, *385*, 263.

[30] B. Huang, J. Malzbender, R. Steinbrech, E. Wessel, H. Penkalla, L. Singheiser, *J. Membr. Sci.* **2010**, *349*, 183.

[31] G. Pećanac, S. Foghmoes, M. Lipińska-Chwałek, S. Baumann, T. Beck, J. Malzbender, *J. Eur. Ceram. Soc.* **2013**, *33*, 2689.

[32] J. Malzbender, *Ceram. Int.* **2016**, *42*, 7899.

[33] R. O. Silva, J. Malzbender, F. Schulze-Küppers, S. Baumann, O. Guillon, *J. Eur. Ceram. Soc.* **2017**, *37*, 2629.

[34] T. Nithyanantham, S. Bandopadhyay, in *Advances in Solid Oxide Fuel Cells III :Ceramic and Engineering Science Proc.* (Eds: N. P. Bansal, J. Salem, D. Zhu), Vol. *28*, Wiley, Florida **2007**, p. 377.

[35] T. Nithyanantham, S. Biswas, N. Nagendra, S. Bandopadhyay, *Ceram. Int.* **2014**, *40*, 7783.

[36] E. Broitman, *Tribol. Lett.* **2017**, *65*, 23.

[37] P. Haušild, A. Materna, L. Kocmanová, J. Matějíček, *J. Mater. Res.* **2016**, *31*, 3538.

[38] N. X. Randall, M. Vandamme, F.-J. Ulm, *J. Mater. Res.* **2009**, *24*, 679.

[39] J. Menčík, *Nanoindentation Mater. Sci.* **2012**, *54*, 53.

[40] G. Constantinides, K. R. Chandran, F.-J. Ulm, K. Van Vliet, *Mater. Sci. Eng.: A* **2006**, *430*, 189.

[41] R. Pal, *J. Compos. Mater.* **2005**, *39*, 1147.

[42] C. Kleinlogel, L. J. Gauckler, *Solid State Ionics* **2000**, *135*, 567.

[43] S. M. Hartig, *Curr. Protoc. Mol. Biol.* **2013**, *102*, 14.

[44] T. W. Ridler, S. Calvard, *IEEE Trans. Syst. Man Cybern.* **1978**, *8*, 630.

[45] ASTM International, *ASTM E2546-15 Standard Practice for Instrumented Indentation Testing*, ASTM International, West Conshohocken, PA **2015**.

[46] W. C. Oliver, G. M. Pharr, *J. Mater. Res.* **1992**, *7*, 1564.